

Ir(III) Based Phosphors with Bi-pyrazolate Ancillaries; Rational Design, Photophysics and Applications in Organic Light Emitting Diodes

Jia-Ling Liao,^a Yun Chi,^{a,*} Zong-Ting Sie,^b Chia-Hao Ku,^b Chih-Hao Chang,^{b,*} Mark A. Fox,^c Paul J. Low,^{d,*} Meu-Rung Tseng^e and Gene-Hsiang Lee^f

^a Department of Chemistry and Low Carbon Energy Research Center, National Tsing Hua University, Hsinchu 30013, Taiwan; E-mail: ychi@mx.nthu.edu.tw

^b Department of Photonics Engineering, Yuan Ze University, Chungli 32003, Taiwan; E-mail: chc@saturn.yzu.edu.tw

^c Department of Chemistry, Durham University, South Rd, Durham, DH1 3LE, UK.

^d School of Chemistry and Biochemistry, University of Western Australia, 35 Stirling Highway, Crawley, 6009, Western Australia, Australia; E-mail: paul.low@uwa.edu.au

^e Material and Chemical Research Laboratories, Industrial Technology Research Institute, Hsinchu 31040, Taiwan.

^f Instrumentation Center, National Taiwan University, Taipei 10617, Taiwan.

Abstract

A series of three charge-neutral Ir(III) complexes bearing both 4,4'-di-*t*-butyl-2,2'-bipyridine (dtbbpy) and cyclometalate such as 2-phenylpyridine (ppyH), together with two monoanionic ligands (i.e. chloride and monodentate pyrazolate) or a single dianionic chelate derived from either 5,5'-di(trifluoromethyl)-3,3'-bipyrazole (bipzH₂) or 5,5'-(1-methylethylidene)-bis(3-trifluoromethyl-1H-pyrazole) (mepzH₂), were successfully synthesized. These complexes are derived from a common structurally characterized, intermediate complex [Ir(dtbbpy)(ppy)Cl₂] (**1**), which represent an unique Ir(III) intermediate complex formed by treatment of IrCl₃·3H₂O with equal amount of diimine (N[^]N) and cyclometalate (C[^]N) chelates in a form of one-pot

reaction. Furthermore, treatment of **1** with various functional pyrazoles afforded [Ir(dtbbpy)(ppy)(pz)Cl] (**2**), [Ir(dtbbpy)(ppy)(bipz)] (**3**) and [Ir(dtbbpy)(ppy)(mepz)] (**4**), which display intense room temperature emission with λ_{max} spanning the region between 532 ~ 593 nm in both fluid and solid states. The Ir(III) complexes, **3** and **4**, showcase rare examples of three distinctive chelates (i.e. neutral, anionic and dianionic) assembling around the central Ir(III) cation. Hybrid-DFT (B3LYP) electronic structure calculations on **1** – **4** reveal the LUMO to be $\pi^*(\text{bpy})$ for all complexes and HOMO at $d(\text{Ir})-\pi(\text{phenyl})$ for **1**, **2** and **4** and at $\pi(\text{bipz})$ for **3**. The different MO make-ups in **3** and **4** are confirmed using pure DFT (BLYP) and wavefunction (MP2) methods here. On the basis of TD-DFT calculations, the emissions are dominated by the phenyl group-to-bipyridine, $\text{ligand}_{(\text{ppy})}$ -to- $\text{ligand}_{(\text{bpy})}$ charge transfer ($^3\text{LLCT}$) admixed with MLCT transition for all Ir(III) complexes. In addition, fabrications of organic light emitting diodes (OLEDs) were successfully accomplished. A double emitting layer design was adopted in the device architecture using Ir(III) metal complexes **3** and **4**, attaining peak external quantum efficiencies, luminance efficiencies, and power efficiencies of 18.1% (58.6 cd/A and 38.6 lm/W) and 16.4% (51.6 cd/A and 28.9 lm/W), respectively.

Introduction

In the last three decades, a large number of third-row transition-metal complexes showing strong photoluminescence in both fluid and solid states have been extensively investigated, with studies of their basic photophysical properties leading to possible use of such complexes in the fabrication of optoelectronic devices, especially organic light emitting diodes (OLEDs).¹⁻⁹ The chelating ligands are known to control both intermolecular interactions through steric constraints and electrical characteristics. Hence, both variation of the metal-ligand bond strength though choice of donor atoms of the chelates and addition of dendritic functional

appendages, have proved highly valuable as part of the complex design strategy.^{10,11} In addition to improved luminescent efficiency, the appropriate choice of ligand can also permit tuning of the emission color, as well as improving various physical and chemical properties, such as thermal and photo stability and solubility, which are important for device fabrication.¹² Among the numerous chelating ligand designs which have been explored to date, 2,2'-bipyridine (Chart 1) and analogous neutral diimines have been employed in the construction of ionic metal-based phosphors as suitable candidates for fabrication of light emitting electrochemical cells (LECs).¹³⁻¹⁶

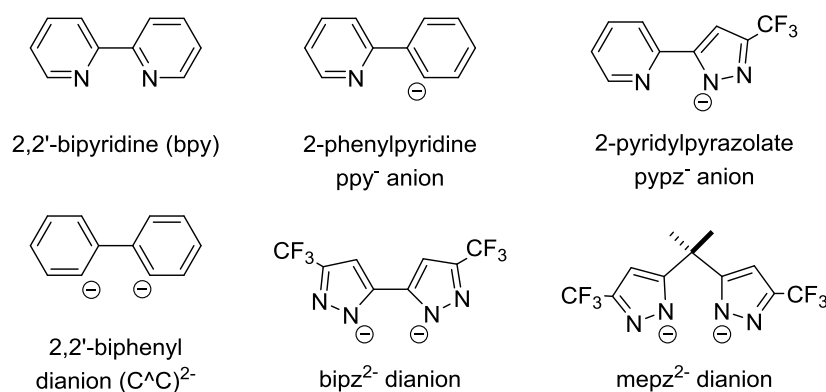


Chart 1: Chelating ligands with varying electronic character.

In sharp contrast, 2-phenylpyridine (ppyH) and its analogues often react with transition metal complexes via cyclometalation processes, and serve as a class of monoanionic *C,N*-chelates (Chart 1).¹⁷ Through consideration of the fine balance of metallic and net ligand charge(s), charge-neutral complexes can be accessed. The neutral formulation and generally high thermal stability and volatility of these complexes makes them well suited for deposition in OLED device structures through thermal evaporation methods.

In comparison with the large number of complexes derived from *ortho*-metalated 2-phenylpyridine and derivatives, examples featuring dianionic chelate ligands are relatively rare. Examples of dianionic chelating ligands include the 2,2'-biphenyl dianion (Chart 1)^{18,19} and benzene-1,2-dithiolate,²⁰ which have been

successfully applied in the syntheses of heteroleptic Pt(II) and Ir(III) metal phosphors, in various combinations with neutral diimine and / or monoanionic cyclometalating chelates. Computational analyses of complexes bearing this class of dianionic chelate suggested that the occupied frontier orbitals primarily contain electronic contributions from the metal atom and the dianionic chelate, while the unoccupied frontier orbitals reside on chelating ligand(s) with less anionic character.¹⁹ Hence, the lower energy optical transitions are often best described as metal-ligand-to-ligand charge transfers (MLLCT), and which may be distinguished in character from more typical ligand-centered (LC) $\pi\pi^*$ and metal-to-ligand charge transfer (MLCT) transitions in metal complexes.

Parallel to the development of metal phosphors containing chelating diimine and cyclometalated ligands, our group has been interested in metal phosphors containing monoanionic pyridyl pyrazolate ligands (pypz⁻, Chart 1), which offer bonding character closely related to the previously mentioned cyclometalates (e.g. ppy⁻, Chart 1).²¹⁻²⁴ In seeking to further extend the synthetic scope of functional chelating ligands, we were drawn to 5,5'-di(trifluoromethyl)-3,3'-bi-pyrazole (bipzH₂)²⁵ and 5,5'-(1-methylethylidene)-bis(3-trifluoromethyl-1H-pyrazole) (mepzH₂) by removal of the two acidic protons to give rise to the associated dianionic chelate ligands (bipz²⁻ and mepz²⁻ respectively, Chart 1). In fact, bipz chelate and analogues have been used to afford many Os(II) and Ru(II) metal complexes which exhibit strong near-infrared (NIR) emission^{26,27} and planar Pt(II) metal complexes with strong solid-state $\pi\pi$ -stacking interaction,²⁸ and to serve as efficient sensitizers for dye-sensitized solar cells (DSSC), respectively.²⁹ In this study, we have examined the use of the dianionic bipz and mepz chelates as constituents in the design of Ir(III) phosphors, which can serve as decent dopant emitters in OLED devices.

Results and Discussion

Syntheses and Characterization. It has been reported that IrCl₃·nH₂O reacts

with 2 equivalents of 2-phenylpyridine or derivatives, described by the general abbreviation (C^N)H, in refluxing 2-ethoxyethanol to afford an chloride-bridged dimer with general formula [(C^N)₂Ir(μ-Cl)]₂ in high yields.³⁰ Structural studies show that each Ir(III) metal center is coordinated by two C^N cyclometalates and two *cis*-arranged bridging chlorides.³¹⁻³³ The halide bridges are formed to compensate for the coordinative unsaturation of the five-coordinate species [(C^N)₂IrCl] generated during the reaction.³⁴ While formation of cationic bis-diimine Ir(III) complexes [Ir(N^N)₂Cl₂]⁺ have been documented (e.g. N^N = bpy, Chart 1),^{35,36} surprisingly there is no precedent on the formation of charge neutral [Ir(N^N)(C^N)Cl₂] by replacement of one diimine chelate (N^N) with the cyclometalate chelate (C^N) during assembly of metal complexes.

Here, the reaction of IrCl₃·nH₂O with one equivalent of neutral diimine (N^N) and heteroaromatic cyclometalate pro-ligand, (C^N)H, was explored with the aim of producing the Ir(III) complexes of formula [Ir(N^N)(C^N)Cl₂] directly, which might also serve as a reactive intermediate in the preparation of tris-heteroleptic complexes. Thus, treatment of IrCl₃·nH₂O with a 1:1 mixture of 4,4'-di-*t*-butyl-2,2'-bipyridine (dtbbpy) and 2-phenylpyridine (ppyH) afforded [Ir(dtbbpy)(ppy)Cl₂] (**1**) as a light orange solid in 60% yield.

Synthetic attempts to replace both chloride ligands in **1** with strongly π-accepting anions such as the pyrazolate, pz = 3-CF₃C₃N₂⁻, were also examined. However, reaction of **1** with Na[3-CF₃C₃N₂] gave only moderate yields of the mono-substituted product [Ir(dtbbpy)(ppy)(pz)Cl] (**2**) (35%). No further substitution could be observed, despite addition of excess Na[3-CF₃C₃N₂], increased reaction temperatures or extended reaction times.³⁷ In contrast, reactions of **1** with the di-sodium salts of the chelating bis(pyrazolate) ligands, 5,5'-di(trifluoromethyl)-3,3'-bipyrazolate (bipz) and 5,5'-(1-methylethylidene)-bis(3-trifluoromethyl-pyrazolate) (mepz), resulted in substitution of both chloride ligands to form the mononuclear Ir(III) complexes [Ir(dtbbpy)(ppy)(bipz)] (**3**) and

[Ir(dtbbpy)(ppy)(mepz)] (**4**) in high yields (75 – 78%). The Ir(III) metal complexes **1**, **3** and **4** were purified using routine silica gel column chromatography, followed by recrystallization, while **2** was isolated by simple washing with a mixture of water and acetone due to its poor stability in contact with the silica gel. The ^1H NMR spectra of each of the complexes **1** – **4** showed non-equivalent signals from the *t*-butyl protons, consistent with the lack of symmetry in all complexes due to the asymmetric phenylpyridyl chelate present. The geometries for **1**, **3** and **4** are confirmed by X-ray crystallography (*vide infra*) whereas the geometry for **2** is assumed on the basis of computations (*vide infra*) and shown in Chart 2.

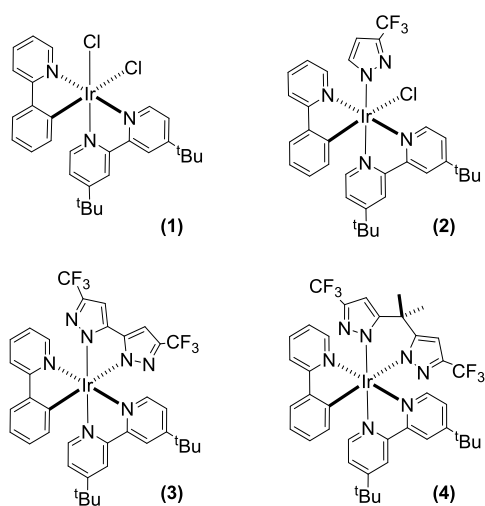


Chart 2: Ir(III) complexes **1** – **4** investigated in this study.

Single crystal X-ray diffraction studies on Ir(III) metal complexes **1**, **3** and **4** confirmed the identification of isomers and showed the influence of the anionic ancillaries imposed on the metal coordination framework. As shown in Figure 1, complex **1** exhibits a slightly distorted octahedral arrangement with the *cis*-disposed chloride ligands, where bite angles of both C^N and N^N chelates (80.4(3) and 79.4(2)^o) are found to be more acute than the unconstrained Cl(1)-Ir-Cl(2) angle of 90.29(6)^o. The Ir-Cl(1) distance (2.3564(16) Å) is notably shorter than the second Ir-Cl(2) distance (2.4898(17) Å), due to the increased *trans*-effect of the unique

phenyl fragment.³⁸ However, the longer Ir-Cl distance in **1** is comparable to the Ir-Cl distances (~ 2.50 Å) observed in the dimer $[\text{Ir}(\text{C}^{\wedge}\text{N})_2(\mu\text{-Cl})_2]$, in which all chlorides are located opposite to the carbon atoms of cyclometalate chelates.³¹⁻³³

The molecular structures of the Ir(III) complexes **3** and **4** are depicted in Figures 2 and 3, respectively, and, together with the structure of **1**, illustrate the different *trans*-influence imposed by the various ligands. The Ir-C(1) (2.028(4) Å) and Ir-N(7) (2.041(4) Å) bonds in **3**, and the corresponding Ir-C(1) (2.020(4) Å) and Ir-N(3) (2.025(3) Å) bonds in **4**, all are located *trans* to the pyrazolate fragments and showed an elongation versus the comparable metal-ligand distances in **1**, cf. Ir-C(1) = 1.999(7) and Ir-N(3) = 2.010(5) Å. These changes can be understood in terms of the increased *trans*-influence of the π -accepting but strongly σ -donating pyrazolates versus that of the inductively electron σ -withdrawing and π -donating chloride ligands.

In the structures of complexes **3** and **4**, the longest Ir-N bond distance is found to be *trans* to the Ir-C bond confirming the orientation of the ppy ligand with respect to other chelating ligands in the structure. The N-Ir-N bite angle of bipz chelate in **3** ($77.07(14)^\circ$) is more acute than that observed for mepz chelate of **4** ($86.95(13)^\circ$). The smaller bite angle is due to the formation of fused pyrazolate-metallacycle-pyrazolate coordination architecture of the bipz chelate in a planar arrangement in **3**, whereas the mepz architecture in **4** is puckered due to the existence of the methylene spacer.

Photophysical data. The absorption and emission spectra of Ir(III) complexes **1** – **4** in CH_2Cl_2 are shown in Figure 4, while Table 1 lists the corresponding numerical data. In general, the strong absorption bands above 300 nm are assigned to the spin-allowed ligand centered $^1\pi\pi^*$ transition. The next lower energy absorptions with maxima around ~ 375 nm can be ascribed to a combination of spin-allowed metal-to-ligand charge transfer ($^1\text{MLCT}$) and metal-ligand-to-ligand charge transfer ($^1\text{MLLCT}$) transitions. The lowest energy band with peak maxima at 454 ~ 468 nm and with relatively small absorptivity is assigned to the spin-orbit coupling enhanced

transitions with $^3\text{MLCT}$ and $^3\text{MLLCT}$ characters. In comparison to complexes **3** and **4** with the bipyrazolate chelate, both complexes **1** and **2** showed more red-shifted absorption peak, with onset at ~ 540 nm, confirming the π -donor property of the chloride versus the π -acceptor character of the bipyrazolate fragment.

Intense orange emissions were observed for **1** and **2** in degassed CH_2Cl_2 with peak wavelengths at 597 nm and 593 nm, respectively. The observed lifetimes of ca. 816 and 799 ns, in combination with the emission quantum yield (Φ) of 0.24 and 0.23, lead us to deduce radiative rate constants of 2.94×10^5 and $2.88 \times 10^5 \text{ s}^{-1}$ for **1** and **2**, respectively. Complex **3** with the bipz chelate reveals a blue-shifted emission with $\lambda_{\text{max}} \sim 546$ nm, together with a slightly shortened lifetime of 355 ns and a comparable quantum yield, $\Phi = 0.27$. In sharp contrast, complex **4** with the mepz chelate exhibits a significantly longer lifetime of 2.27 μs and Φ of 0.76. On the other hand, the chloride ligand present in both complexes **1** and **2** is a π -donating and weak field ligand, which is expected to stabilize the metal-centered MC dd excited state. The reduced energy gap between the emitting state and MC dd excited state would induce faster thermal population to the higher lying dd state and, hence, reduce the emission quantum yield due to the faster deactivation channel. Interestingly, the emission quantum yield for **3** is substantially higher ($\Phi = 0.73$) than the other complexes in the solid state. This enhancement could be caused by the more rigid media that effectively suppressed the large-amplitude vibrations or temporal dissociation of the bipz chelate from the metal coordination sphere.³⁹

Electrochemistry. The electrochemical properties of **1** – **4** were examined using cyclic voltammetry (CV). Figure 5 and Table 2 show the voltametric wave profiles and numerical data, respectively. There is only a small variation of the anodic oxidation peak potential as a function of complex composition, suggesting that the stability of the metal centered oxidation is only slightly influenced by the ancillaries, i.e. chloride or pyrazolate.⁴⁰ Basically, only the Ir(III) complex **3** showed a quasi-reversible

oxidation peak that gave a half-wave potential of 0.82 V (vs. the ferrocenium/ferrocene couple at 0.0 V), whereas complexes **1**, **2** and **4** show irreversible oxidation processes with the anodic maxima at 0.80, 0.86 and 0.85 V respectively. It seems that the bipz chelate of **3** is responsible for the higher reversibility to the oxidized species compared to the other complexes.

For the reduction potentials, complexes **1** – **4** showed cathodic peaks of -2.07, -2.07, -2.02 and -2.14 V, respectively. Based on the DFT calculations (*vide infra*), the reduction is expected to occur at the π^* -orbital of bpy ligand with only minor influences from the chloride and/or the pyrazolate. Hence, complexes **1** and **2** exhibited identical cathodic peak potentials, while complexes **3** and **4**, show small but distinctive differences presumably due to the presence and absence of extended π -conjugation on the bipz and mepz chelates, respectively. The potential differences between the observed anodic oxidation and cathodic reduction potentials are in a narrow range of 2.87 ~ 2.99 V and do not follow the trends of the emission maxima observed for **1** – **4**, among which the difference in potential of **1** is lower than that of **4** by 0.12 V.

DFT calculations. To further investigate the optoelectronic properties of compounds **1** – **4** calculations based on density functional theory (DFT) and time-dependent density functional theory (TD-DFT) were undertaken. The B3LYP functional with a LANL2DZ basis set on Ir and 6-31G** on all other atoms, as well as a conductor-like polarization continuum (CPCM) model of the CH_2Cl_2 solvent were employed. The model structures are denoted **1'** – **4'** to distinguish the computed structural data from that determined by the single crystal X-ray diffraction analyses.

The results from geometry optimizations of **1'** – **4'** are summarized in the captions to Figures S1 – S3 and 6. The majority of differences in bond lengths are within 0.03 Å, although the Ir-Cl distances are over-estimated by 0.1 Å in **1'** in comparison with the crystallographically determined structures where available.³²

While the isomers for **1**, **3** and **4** have been structurally characterized, the geometry for **2** has not been confirmed. Assuming that the ppy and bpy ligands in **1** are retained in the formation of **2** from **1** with the pyrazolate (pz) anion, there are two possible isomers (Figures S1 and S2). The geometry **2'** in Figure 6 is more stable than the other possible isomer by 3.8 kcal mol⁻¹ and is believed to be the thermodynamically most stable isomer in **2**. Relative energies for several possible isomers of **1** – **4** reveal that the geometry observed for **1** is indeed the thermodynamically most stable isomer, but there are more stable isomers for **3** and **4** than the conformers found experimentally (Figures S3 – S4). Thus, the geometries observed experimentally for **3** and **4** are formed kinetically with the retention of ppy and bpy orientations in the syntheses of **3** and **4** upon addition of bipyrazolate chelate to **1**. Moreover, extensive heating of both **3** and **4** for over 24 hours have also produced no isomerization. This observation is in sharp contrast to those observed in several Ir(III) metal complexes, for which excessive heating or sublimation have induced the structural isomerization to give formation of the thermodynamically most stable products.⁴¹⁻⁴³

The target compound **5'** containing two pyrazolates (Figure S5) from the reaction of **1** with excess pyrazolate anion was looked at computationally for an explanation as to why **5** was not formed. Based on the total energies calculated for **1'**, **2'** and **5'**, compound **5** should be formed given that there are no obvious steric hindrances between the two pz ligands in **5'**. It is assumed here that the second pz anion is deterred from replacing the chloride by the more congested pz ligand in **2**. In contrast, [(C[^]N)₂Ir(μ-Cl)]₂ is known to react with pzH in affording both cationic [(C[^]N)₂Ir(pzH)₂]⁺ and neutral [(C[^]N)₂Ir(pzH)(pz)], (C[^]N)H = 2-*p*-tolylpyridine and pzH = C₃N₂H₄,³⁷ for which the smaller pyrazole provided the demanded stabilization for the double chloride-to-pz substitution.

Plots of the HOMO and LUMO of **1'** – **4'** are given in Figure 7, with details of the orbital contribution given in the caption. The LUMO is bpy π*-orbital in character in

all complexes and well isolated from the occupied ($E_{\text{HOMO-LUMO}} = 3.29$ (**1'**), 3.29 (**2'**), 3.01 (**3'**) and 3.43 (**4'**) eV) and other virtual orbitals ($E_{\text{LUMO-(LUMO+1)}} = 0.75$ (**1'**), 0.74 (**2'**), 0.75 (**3'**) and 0.72 (**4'**) eV).

In the case of **1'**, **2'** and **4'**, the HOMO is predominantly delocalized over the Ir metal atom and the phenyl fragment of ppy ligand with energies at -5.66 , -5.64 and -5.71 eV respectively with a moderate (12 – 15%) contribution from the chloride(s) in the case of **1'** and **2'**. For **3'** the HOMO is on the bipz chelate at a considerably higher energy of -5.39 eV (Figure 7). Given that the electrochemical oxidation and photochemical data for **3** are similar to those for **1**, **2** and **4**, the calculated HOMO forms and energies should also be similar in all cases. The orbital make-ups for **3'** and **4'** remain unchanged using a range of 'pure' DFT (BLYP), hybrid functionals (PBE0, wB97) and 'pure' wavefunction HF, MP2 methods, with different basis sets, pseudopotentials and solvation methods (Table S1). Unless there is a remarkable systematic error in high-level ab initio and DFT computations,^{44,45} the orbital make-ups for **3'** and **4'** appear to be valid here. The HOMO-1 for **3'** is predominantly delocalized over the Ir metal atom and the phenyl fragment of ppy ligand (Figure 7) with a similar energy (-5.83 eV) as the HOMO energies for **1'**, **2'** and **4'**.

In considering their absorption data in solution it is apparent that the complexes fall into two groups: the chloro containing complexes **1** and **2** with lower energy absorption maxima than the bis(pyrazolate) complexes **3** and **4** (Figure 4, Table 1). These observations are well matched by trends in the results from time-dependent density functional calculations (TD-DFT) from **1'**, **2'**, **3'** and **4'**, which are summarized in Table 3, together with lists of the energy and orbital analyses of the lowest energy singlet and triplet transitions. The agreement between the calculated $S_0 \rightarrow S_n$ transition energies and the observed absorption bands are very good (Figure 8) even though the calculated energies of the $S_0 \rightarrow T_1$ transitions have zero oscillator strengths as the transitions are forbidden and the calculations do not allow for spin-orbit couplings. The observed lowest energy absorption features are,

unsurprisingly, attributed to the HOMO \rightarrow LUMO transitions (HOMO-1 \rightarrow LUMO in the case of **3'**), and therefore have considerable $ML_{(bpy)}CT$ character as well as the metal-halide-to-ligand charge transfer character (MXLCT) in the case of **1'** and **2'**.

Predicted phosphorescence emission data should be obtained from TDDFT data on optimized T_1 geometries but open-shell geometry optimizations (excited states e.g. S_n , T_n $n > 0$) on iridium complexes are generally unreliable and the TDDFT data from these optimized geometries are poor as a result (Table S2).⁴⁶ [46. Tavasli, M.; Moore, T. N.; Zheng, Y.; Bryce, M. R.; Fox, M. A.; Griffiths, G. C.; Jankus, V.; Al-Attar, H. A.; Monkman, A. P. J. Mater. Chem. 2012, 22, 6419. Can you add this reference please and change the subsequent reference numbers as your citation set-up is different to my set-up?] The predicted emission maxima are more accurate from TDDFT data on S_0 optimized geometries with the reverse processes of the $S_0 \rightarrow S_n/T_n$ transitions than TDDFT data from optimized excited state geometries. This is particularly true when i) the nature of the emissions are similar to that of the corresponding absorptions, ii) the S_0 and T_1 geometries are similar and iii) the calculated transitions are adjusted with an appropriate Stokes shift energy constant.⁴⁶

The calculated $S_0 \rightarrow T_1$ transition wavelengths here do not take into account the Stokes shifts expected experimentally resulting in the predicted emission energies being overestimated but they do follow the trend in emission maxima (Table 3) except for **3'**. The emissions correspond to the reverse processes of the $S_0 \rightarrow T_1$ transitions in **1'** and **2'**, admixed with a 10% component from the mepz ligand in the case of **4'**. The mepz ligand is presumably responsible for the longer emission lifetime in **4**. It is very likely that the observed emission in **3** is attributed to a $ML_{(bpy)}CT$ character with a bipz component as it is phosphorescence which implies that the metal is involved. Assuming that the HOMO in **3'** is on the bipz ligand, it could be argued that the HOMO-1 \rightarrow LUMO ($S_0 \rightarrow S_2$) process in **3** at *ca* 450 nm excitation gives a second singlet excited state (S_2). This singlet state, involving the oxidation of the iridium-phenyl moiety, results in a triplet excited state via an intersystem crossing

(ISC) pathway. This assumption is supported by spin density calculations on the S_1 and T_1 optimized geometries of **3'** where the spin densities are largely located on the ligands and not on the metal (Figure S6 and Table S3). The triplet state formed from the ISC of the metal-dominated excited singlet state (S_2) is probably responsible for the phosphorescence observed in **3** experimentally (Figure S7 and Table S3).

OLED Device Fabrication. To investigate the electroluminescent performances of these Ir(III) complexes, the device architecture using Ir(III) complex **3** as the dopant was first optimized. The same architecture was then applied to other phosphors **4** and **1** for comparison purposes. In general, host materials for green or yellow emitting phosphors should possess triplet energy gaps greater than 2.5 eV, to ensure adequate energy transfer as well as exciton confinement.⁴⁶ Furthermore, hosts with bipolar transport capability are expected to allow fine adjustment of carrier transport and recombination.⁴⁷ Consequently, we tested three potential bipolar hosts with suitable triplet energy gaps; namely: 4,4'-Bis(N-carbazolyl)-1,1'-biphenyl (CBP),⁴⁸ 1,3-bis(9-carbazolyl)benzene (mCP),⁴⁹ and 2,6-Bis(3-(9H-carbazol-9-yl)phenyl)pyridine (26DCzPPy).⁵⁰ The compounds 1,1-bis[(di-4-tolylamino)phenyl]cyclohexane (TAPC) and 3,5,3',5'-tetra(m-pyrid-3-yl)-phenyl[1,1']biphenyl (BP4mPy) were chosen to serve as the hole-transport layer (HTL) and the electron-transport layer (ETL), respectively.^{51,52} Experimental data on devices with the mCP and 26DCzPPy hosts show external quantum efficiencies of 14.1% and 15.6% (see details given in SI, Figure S8 and Table S4), which are notably higher than that for a device fabricated with the CBP host (i.e. 8.7%). Although the device formed with 26DCzPPy exhibited adequate efficiency, the turn-on voltage increased to 6.2 V, as well as giving a pronounced efficiency roll-off at the higher driving voltages. Thus, for lowering the operation voltage and achieving high efficiency, architecture based double emitting layers (EMLs) were investigated.⁵³

To form the test double EML devices, the OLED structures were changed to ITO/

TAPC (40 nm)/ mCP & **3** (x nm)/ 26DCzPPy & **3** (30- x nm)/ BP4mPy (40 nm)/ LiF (0.8 nm)/ Al (150 nm), where LiF and aluminum are utilized as the electron injection layer and reflective cathode, respectively. Optimization of EML layers were also executed, where the best device data is obtained with $x = 15$ nm and with doping level of 4 wt.%. Figure 9 presents the schematic device architecture, the molecular drawings and the energy diagram of the materials employed. Studies were also extended to OLED devices with relevant dopants **4** and **1**. The combined OLED performances are summarized in Figure 10 and Table 4.

Devices A, B and C represent devices fabricated using dopants **3**, **4** and **1**. The electroluminescent (EL) spectra shown in Figure 10(a) were identical to the respective PL spectra recorded in the solution state, indicating effective exothermic energy transfer from the hosts (i.e. mCP and 26DCzPPy) to the dopants.⁵⁴ The EL emission of device C (with dopant **1**) is notably red-shifted from the bipyrazolate complexes **3** and **4**, and this is consistent with the lowered energy gap recorded in solution. Furthermore, the double EMLs would expand the emission zone, leading to a lower exciton density compared to the traditional, single EML devices. Thus, the triplet-triplet annihilation can be effectively suppressed to give improved device efficiencies.⁵⁵

The current density-voltage (J - V) curves of tested devices follow in descending order: $A > C > B$ (Figure 10(b)). In general, dopants with a lower energy gap would induce rapid carrier trapping in EML (especially for dopants with poor carrier transport abilities).^{56,57} In comparison to device C with dopant **1**, the lower current density of device B revealed the negative influence of mepz chelate in **4**, on carrier transport and recombination. In contrast, complex **3** with the bipz chelate possesses the best carrier transport capability among all three devices. The turn-on voltages of devices A, B and C were measured to be at 4.8, 5.0, and 5.4 V, respectively. Similarly, device A showed a max. luminance of 84899 cd/m^2 at an operating voltage of 15.4 V, while device B only achieved a max. luminance of 48305 cd/m^2 at 16.6 V. As expected,

due to the lowered photoluminescent Φ of **1** in solid state, device C exhibited the worst max. luminance of 32665 cd/m² at 16.2 V.

The external quantum efficiencies, the luminance data and power efficiencies are depicted in Figures 10(c) and 10(d). Similarly, device C has the lowest peak efficiencies, which can be ascribed to the lower Φ of **1** (i.e. 24%). In addition, the peak efficiencies of devices A and B reached 18.1% (58.6 cd/A and 38.6 lm/W) and 16.4% (51.6 cd/A and 28.9 lm/W), respectively. These outcomes suggest a nearly unitary internal quantum efficiency and good carrier balance in both devices A and B. Furthermore, device A maintained forward efficiencies of 17.6 %, 57.4 cd/A, and 30.0 lm/W at 100 cd/m²; while device B gave forward efficiencies of 15.2%, 49.9 cd/A, and 22.4 lm/W. Overall, these data indicate the high potential of Ir(III) metal complexes **3** and **4** for use in display and lighting applications, confirming the advantage of employing the bipz and mepz chelate in assembly of the Ir(III) metal based phosphors.

Conclusions

In summary, a new series of Ir(III) metal based phosphors with three bidentate chelates that consist of diimine, cyclometalate and bis-pyrazolate were synthesized and characterized. Of particular interest is the complexes **3** and **4**, each with bipz or mepz chelate, which showcase a rare example, with three distinctive chelates (i.e. neutral, anionic and dianionic) assembling around the central Ir(III) metal cation. TD-DFT calculations indicate emissions to largely originate from ³MLCT processes, admixed with ³MXLCT in the case of the chloride-containing complexes **1** and **2**. As for the bis-pyrazolate complexes **3** and **4**, the emissions are significantly blue-shifted and with improved emission quantum yields. The Ir(III) complexes were examined for their potential in optoelectronic applications, particularly in the fabrication of OLED devices. With the double EMLs design, the respective peak efficiencies of phosphorescent OLEDs with Ir(III) metal complexes **3** and **4** were respectively

recorded at 18.1% (58.6 cd/A and 38.6 lm/W) and 16.4% (51.6 cd/A and 28.9 lm/W), confirming their promising device characteristics.

Experimental Section

General Information and Materials. Mass spectra were obtained on a JEOL SX-102A instrument operating in electron impact (EI) mode or fast atom bombardment (FAB) mode. ^1H , ^{19}F NMR spectra were obtained using the Varian Mercury-400 instruments. Elemental analyses were performed using the Heraeus CHN-O rapid elementary analyzer. 5,5'-di(trifluoromethyl)-3,3'-bipyrazole (bipzH₂) was prepared according to literature procedure,²⁹ while 5,5'-(1-methylethylidene)-bis(3-trifluoromethyl-1H-pyrazole) (mepzH₂) was synthesized from condensation of ethyl trifluoroacetate and 3,3-dimethylpentane-2,4-dione, followed by hydrazine cyclization. All reactions were carried out under N₂ atmosphere and anhydrous conditions.

Photophysical measurement. Steady-state absorption and emission spectra were recorded by a Hitachi (U-3900) spectrophotometer and an Edinburgh (FLS920) fluorimeter, respectively. Solutions were degassed by three freeze-pump-thaw cycles prior to measurement of photoluminescence quantum yield (Φ), with an ethanol solution of Coumarin 530 ($\Phi = 0.58$) used as standard. The quantum yield of complexes immobilized in PMMA thin films were measured using an integrating sphere. Lifetime studies were performed by an Edinburgh FL 900 photon-counting system with EPL-375 diode laser as the excitation source.

Cyclic voltammetry. The oxidation and reduction measurements were recorded using glassy carbon as the working electrode at the scan rate of 50 mV s⁻¹. All electrochemical potentials were measured in a 0.1 M TBAPF₆ solution in CH₂Cl₂ for both oxidation and reduction reaction, and reported in volts against an Ag/Ag⁺ (0.01 M AgNO₃) reference electrode with ferrocene (FcH) as the internal standard; ΔE_p is defined as E_{pa} (anodic peak potential) – E_{pc} (cathodic peak potential) and these data

are quoted in mV.

Preparation of 1. A mixture of 4,4'-di-*t*-butyl-2,2'-bipyridine (dtbbpy, 169 mg, 0.63 mmol), 2-phenylpyridine (ppyH, 98 mg, 0.63 mmol) and IrCl₃·3H₂O (222 mg, 0.63 mmol) in 20 mL of diethylene glycol methyl ether (DGME) was heated at reflux for 12 hr. After removal of solvent *in vacuo*, the residue was purified by silica gel column chromatography using ethyl acetate/MeOH (10 : 1) as eluent to afford orange [Ir(dtbbpy)(ppy)Cl₂] (255 mg, 0.37 mmol, 60%).

Spectra data of 1: MS (FAB, ¹⁹³Ir): *m/z* 685 [M⁺]; ¹H NMR (400 MHz, CDCl₃, 294K): δ 10.00 (d, *J* = 5.8 Hz, 1H), 9.94 (d, *J* = 6.2 Hz, 1H), 7.99 (d, *J* = 2.0 Hz, 1H), 7.90 ~ 7.87 (m, 2H), 7.78 (td, *J* = 8.0, 1.6 Hz, 1H), 7.64 (dd, *J* = 8.0, 2.0 Hz, 1H), 7.60 (dd, *J* = 8.0, 1.2 Hz, 1H), 7.46 (d, *J* = 6.2 Hz, 1H), 7.30 (td, *J* = 8.0, 1.4 Hz, 1H), 7.05 (dd, *J* = 8.0, 2.0 Hz, 1H), 6.86 (td, *J* = 8.0, 1.2 Hz, 1H), 6.78 (td, *J* = 8.0, 1.4 Hz, 1H), 6.17 (d, *J* = 8.0 Hz, 1H), 1.50 (s, 9H), 1.29 (s, 9H). Anal. Calcd. for C₂₉H₃₂Cl₂IrN₃: N, 6.13; C, 50.80; H, 4.70. Found: N, 6.36; C, 50.35; H, 4.49.

Selected crystal data of 1: C₃₁H₃₄Cl₈IrN₃; M = 924.41; monoclinic; space group = C2/c; *a* = 22.8121(10) Å, *b* = 11.8525(5) Å, *c* = 27.9109(12) Å; β = 103.0378(10)°; *V* = 7352.0(5) Å³; *Z* = 8; ρ_{calcd} = 1.670 Mg·m⁻³; *F*(000) = 3632; crystal size = 0.25 × 0.20 × 0.15 mm³; λ(Mo-K_α) = 0.71073 Å; *T* = 200(2) K; μ = 4.239 mm⁻¹; 27863 reflections collected, 8453 independent reflections (*R*_{int} = 0.0568), GOF = 1.058, final *R*₁[*I* > 2σ(*I*)] = 0.0522 and *wR*₂(all data) = 0.1245.

Preparation of 2. A suspension of NaH (9 mg, 0.38 mmol) in anhydrous THF (5 mL) was treated with 3-trifluoromethylpyrazole (pzH, 30 mg, 0.22 mmol) at 0 °C, and the mixture was stirred for 20 min. After filtration and evaporation of solvent, the resulting pyrazolate salt was transferred to a 50 mL round-bottom flask, together with [Ir(dtbbpy)(ppy)Cl₂] (150 mg, 0.22 mmol) and 30 mL of anhydrous DMF, and the mixture was brought to reflux for 12 h. After removal of solvent, the residue was washed with a mixture of water and acetone to afford yellow colored [Ir(dtbbpy)(ppy)(pz)Cl] (60 mg, 0.08 mmol, 35%).

Spectra data of 2: MS (FAB, ^{193}Ir): m/z 785 [M^+]; ^1H NMR (400 MHz, CDCl_3 , 294K): δ 9.87 (d, $J = 6.2$ Hz, 1H), 8.39 (d, $J = 5.2$ Hz, 1H), 7.97 (s, 1H), 7.91 ~ 7.88 (m, 2H), 7.76 ~ 7.65 (m, 4H), 7.57 (dd, $J = 6.2, 2.0$ Hz, 1H), 7.17 ~ 7.11 (m, 2H), 6.90 (t, $J = 7.3$ Hz, 1H), 6.84 (t, $J = 7.3$ Hz, 1H), 6.29 (s, 1H), 6.25 (d, $J = 7.3$ Hz, 1H), 1.47 (s, 9H), 1.31 (s, 9H). ^{19}F NMR (376 MHz, CDCl_3 , 294K): δ -59.68 (s, 3F). Anal. Calcd. for $\text{C}_{33}\text{H}_{34}\text{ClF}_3\text{IrN}_5$: N, 8.92; C, 50.47; H, 4.36. Found: N, 8.60; C, 50.11; H, 4.05.

Preparation of 3. A suspension of NaH (15 mg, 0.62 mmol) in anhydrous THF (5 mL) was treated with bipzH₂ (71 mg, 0.26 mmol) at 0 °C, and the mixture was stirred for 20 min. After filtration and evaporation of solvent, the resulting pyrazolate salt was transferred to a 50 mL flask, together with $[\text{Ir}(\text{dtbbpy})(\text{ppy})\text{Cl}_2]$ (150 mg, 0.22 mmol) and 30 mL of anhydrous DMF, and the mixture was brought to reflux for 12 h. The product mixture was purified by silica gel column chromatography using a 1 : 1 mixture of ethyl acetate and hexane as the eluent. The yellow crystals of $[\text{Ir}(\text{dtbbpy})(\text{ppy})(\text{bipz})]$ (**3**) were obtained by slow diffusion of hexane into an ethyl acetate solution (149 mg, 0.17 mmol, 78%).

Spectra data of 3: MS (FAB, ^{193}Ir): m/z 883 [M^+]; ^1H NMR (400 MHz, CDCl_3 , 294K): δ 7.99 (d, $J = 12.0$ Hz, 2H), 7.64 (d, $J = 8.0$ Hz, 1H), 7.59 ~ 7.52 (m, 2H), 7.51 (d, $J = 8.0$ Hz, 1H), 7.44 ~ 7.37 (m, 3H), 7.21 (d, $J = 8.0$ Hz, 1H), 6.94 ~ 6.87 (m, 3H), 6.61 (s, 1H), 6.54 (s, 1H), 6.26 (d, $J = 8.0$ Hz, 1H), 1.42 (s, 9H), 1.34 (s, 9H). ^{19}F NMR (376 MHz, CDCl_3 , 294K): δ -59.42 (s, 3F), -59.83 (s, 3F). Anal. Calcd. for $\text{C}_{37}\text{H}_{34}\text{F}_6\text{IrN}_7$: N, 11.10; C, 50.33; H, 3.88. Found: N, 11.07; C, 50.05; H, 3.67.

Selected crystal data of 3: $\text{C}_{41.50}\text{H}_{43}\text{F}_6\text{IrN}_7\text{O}_{1.50}$; $M = 970.03$; triclinic; space group = P-1; $a = 12.7383(6)$ Å, $b = 12.8295(6)$ Å, $c = 14.6989(7)$ Å; $\alpha = 65.3518(9)^\circ$; $\beta = 76.0091(9)^\circ$; $\gamma = 79.6834(11)^\circ$; $V = 2110.18(17)$ Å³; $Z = 2$; $\rho_{\text{calcd}} = 1.527$ Mg·m⁻³; $F(000) = 968$; crystal size = $0.28 \times 0.20 \times 0.12$ mm³; $\lambda(\text{Mo-K}\alpha) = 0.71073$ Å; $T = 150(2)$ K; $\mu = 3.232$ mm⁻¹; 27417 reflections collected, 9673 independent reflections ($R_{\text{int}} = 0.0423$), $\text{GOF} = 1.127$, final $R_1[I > 2\sigma(I)] = 0.0382$ and $wR_2(\text{all data}) = 0.0971$.

Preparation of 4. Yellow colored complex **4** $[\text{Ir}(\text{dtbbpy})(\text{ppy})(\text{mepz})]$ was

prepared from [Ir(dtbbpy)(ppy)Cl₂] (165 mg, 0.24 mmol) and mepzH₂ (79 mg, 0.25 mmol) using the same procedures as described for **3**; yield 75%.

Spectra data of 4: MS (FAB, ¹⁹³Ir): *m/z* 925 [M⁺]; ¹H NMR (400 MHz, CDCl₃, 294K): δ 7.96 (s, 1H), 7.88 (s, 1H), 7.79 (d, *J* = 8.0 Hz, 1H), 7.66 (d, *J* = 6.4 Hz, 1H), 7.61 (d, *J* = 8.0 Hz, 1H), 7.56 (d, *J* = 7.6 Hz, 1H), 7.48 (d, *J* = 6.0 Hz, 1H), 7.37 (d, *J* = 6.0 Hz, 1H), 7.18 (d, *J* = 6.4 Hz, 1H), 6.97 (t, *J* = 7.6 Hz, 1H), 6.88 (t, *J* = 6.8 Hz, 2H), 6.78 (d, *J* = 6.0 Hz, 1H), 6.37 (s, 1H), 6.31 (s, 1H), 6.23 (d, *J* = 7.6 Hz, 1H), 1.62 (s, 3H), 1.42 (s, 9H), 1.41 (s, 3H), 1.34 (s, 9H). ¹⁹F NMR (376 MHz, CDCl₃, 294K): δ -60.22 (s, 3F), -60.24 (s, 3F). Anal. Calcd. for C₄₀H₄₀F₆IrN₇: N, 10.50; C, 55.84; H, 4.84. Found: N, 10.20; C, 55.66; H, 4.57.

Selected crystal data of 4: C_{41.5}H₄₅F₆IrN₇O_{1.50}; M = 972.05; triclinic; space group = P-1; *a* = 9.4572(6) Å, *b* = 14.5674(9) Å, *c* = 15.9333(10) Å; α = 78.1015(12)°; β = 85.8939(12)°; γ = 73.1797(12)°; *V* = 2055.9(2) Å³; *Z* = 2; ρ_{calcd} = 1.570 Mg·m⁻³; *F*(000) = 972; crystal size = 0.26 × 0.24 × 0.21 mm³; λ(Mo-Kα) = 0.71073 Å; T = 200(2) K; μ = 3.317 mm⁻¹; 26619 reflections collected, 9414 independent reflections (*R*_{int} = 0.0287), GOF = 1.094, final *R*₁[*I* > 2σ(*I*)] = 0.0308 and *wR*₂(all data) = 0.0875.

Single Crystal X-Ray Diffraction Studies: Single crystal X-ray diffraction data were measured with a Bruker SMART Apex CCD diffractometer using (Mo-Kα) radiation (λ = 0.71073 Å). The data collection was executed using the SMART program. Cell refinement and data reduction were performed with the SAINT program. An empirical absorption was applied based on the symmetry-equivalent reflections and the SADABS program. The structures were solved using the SHELXS-97 program and refined using the SHELXL-97 program by full-matrix least squares on *F*² values. The structural analysis and molecular graphics were obtained using the SHELXTL program on a PC.⁵⁸ CCDC 1060246 – 1060248 contain the supplementary crystallographic data for this paper.

Computational studies. Calculations were performed with the Gaussian 09 program package,⁵⁹ using the B3LYP functional,^{60,61} LANL2DZ⁶² basis set for iridium

and 6-31G**⁶³ for all other atoms. A conductor-like polarization continuum model CPCM of CH₂Cl₂ solvent was applied to all calculations, and results analyzed further with GaussSum.⁶⁴ Structures obtained were confirmed as true minima by the absence of imaginary frequencies. Calculations were also carried out on **3'** and **4'** with other models (Table S1) to establish the validity of the model chemistry (B3LYP/LANL2DZ:6-31G**/PCM-DCM) used here.

OLED Fabrication. ITO-coated glass substrate and commercial materials were purchased from Nichem and Lumtec. Materials were subjected to temperature-gradient sublimation under high vacuum. The organic and metal layers were deposited by thermal evaporation in a vacuum chamber with a base pressure of < 10⁻⁶ Torr. The deposition system enabled the fabrication of the completed device structure without breaking the vacuum. The bottom-emitting OLED architecture consists of multiple organic layers and a reflective cathode which were consecutively deposited onto the ITO-coated glass substrate. The active area was defined by the shadow mask (2 × 2 mm²). Current density-voltage-luminance characterization was measured using a Keithley 238 current source-measure unit and a Keithley 6485 picoammeter equipped with a calibrated Si-photodiode. The electroluminescent spectra were recorded using an Ocean Optics spectrometer.

Supporting information. CIF data of Ir(III) complexes **1**, **3** and **4**, proposed isomeric structures, predicted emission and spin density data from optimized S₁, S₂ and T₁ geometries for **1'** – **4'**, cartesian coordinates of the S₀ optimized geometries for the studied Ir(III) complexes **1'** – **4'**, and the device data of OLEDs with single EML structure.

Acknowledgments. This work was supported by the Ministry of Science and Technology of Taiwan, under the grant numbers 102-2221-E-155-080-MY3. P.J.L.

gratefully acknowledges support from the Australian Research Council and the award of a Future Fellowship [FT120100073].

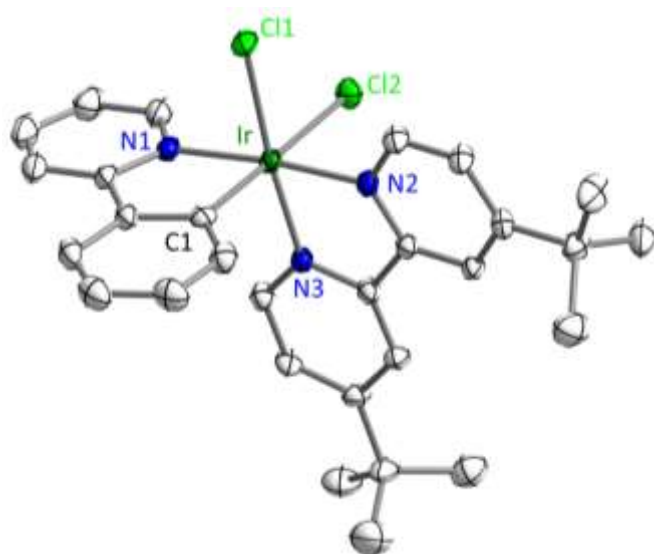


Figure 1. Structural drawing of complex **1** with thermal ellipsoids shown at 30% probability level; selected bond distances: Ir-N(1) = 2.050(5), Ir-N(2) = 2.027(5), Ir-N(3) = 2.010(5), Ir-Cl(1) = 2.3564(16), Ir-Cl(2) = 2.4898(17), and Ir-C(1) = 1.999(7) Å; selected bond angles: N(1)-Ir-C(1) = 80.4(3), N(2)-Ir-N(3) = 79.4(2), and Cl(1)-Ir-Cl(2) = 90.29(6)°. Optimized geometry data: Ir-N(1) = 2.079, Ir-N(2) = 2.062, Ir-N(3) = 2.042, Ir-Cl(1) = 2.4487, Ir-Cl(2) = 2.600, and Ir-C(1) = 2.017 Å; selected bond angles: N(1)-Ir-C(1) = 87.02, N(2)-Ir-N(3) = 78.99, and Cl(1)-Ir-Cl(2) = 91.34°.

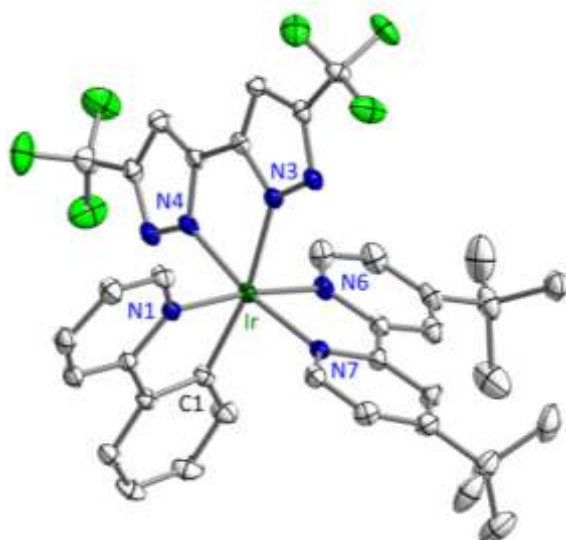


Figure 2. Structural drawing of complex **3** with thermal ellipsoids shown at 30% probability level; selected bond distances: Ir-N(1) = 2.045(4), Ir-C(1) = 2.028(4), Ir-N(6) = 2.028(4), Ir-N(7) = 2.041(4), Ir-N(3) = 2.129(4), and Ir-N(4) = 2.032(4) Å; selected bond angles: N(1)-Ir-C(1) = 80.21(17), N(6)-Ir-N(7) = 79.22(15), and N(3)-Ir-N(4) = 77.07(14)^o. Optimized geometrical data: Ir-N(1) = 2.080, Ir-C(1) = 2.036, Ir-N(6) = 2.059, Ir-N(7) = 2.076, Ir-N(3) = 2.173, and Ir-N(4) = 2.061 Å; selected bond angles: N(1)-Ir-C(1) = 80.06, N(6)-Ir-N(7) = 78.63, and N(3)-Ir-N(4) = 76.75^o.

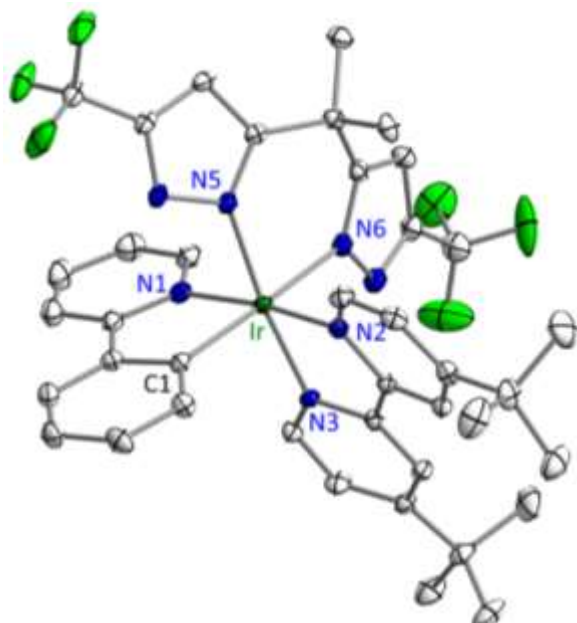


Figure 3. Structural drawing of complex **4** with thermal ellipsoids shown at 30% probability level; selected bond distances: Ir-N(1) = 2.051(3), Ir-N(2) = 2.033(3), Ir-N(3) = 2.025(3), Ir-N(5) = 2.051(3), Ir-N(6) = 2.130(3), and Ir-C(1) = 2.020(4) Å; selected bond angles: N(1)-Ir-C(1) = 80.41(15), N(2)-Ir-N(3) = 79.59(13), and N(5)-Ir-N(6) = 86.95(13)°. Optimized geometrical data: Ir-N(1) = 2.084, Ir-N(2) = 2.059, Ir-N(3) = 2.075, Ir-N(5) = 2.071, Ir-N(6) = 2.163, and Ir-C(1) = 2.040 Å; selected bond angles: N(1)-Ir-C(1) = 80.08, N(2)-Ir-N(3) = 78.59, and N(5)-Ir-N(6) = 86.50°.

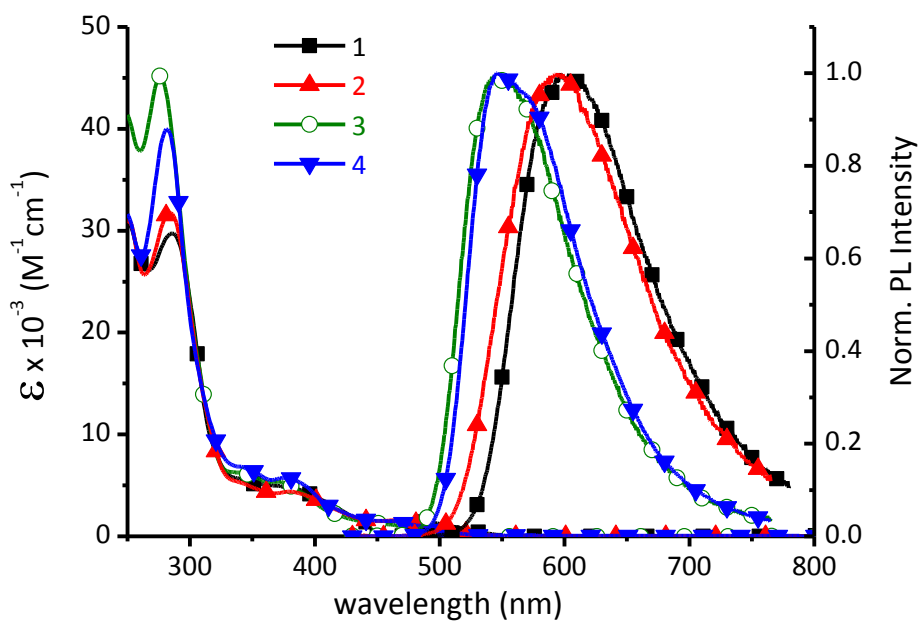


Figure 4. Absorption and normalized emission spectra of Ir(III) complexes recorded in degassed CH_2Cl_2 solution at RT. (ϵ : molar extinction coefficient)

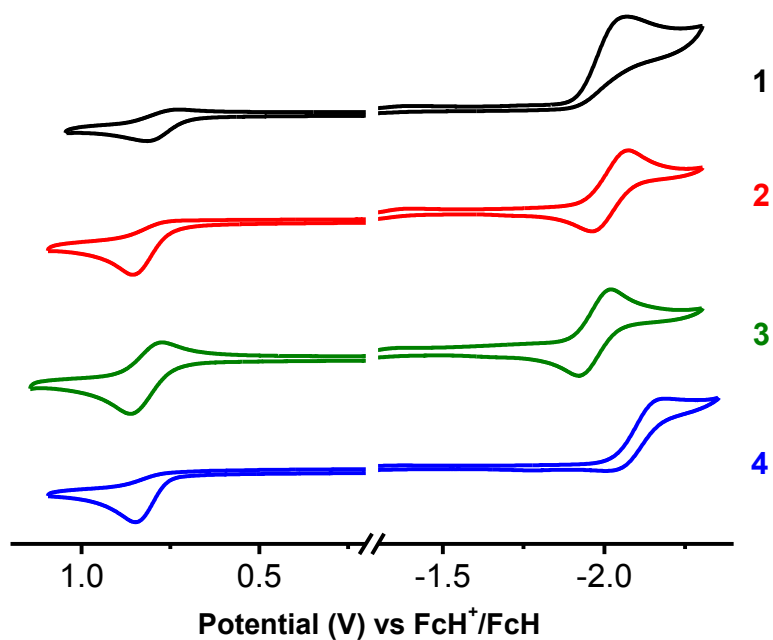


Figure 5. Cyclic voltammograms of the studied Ir(III) complexes **1** – **4**.

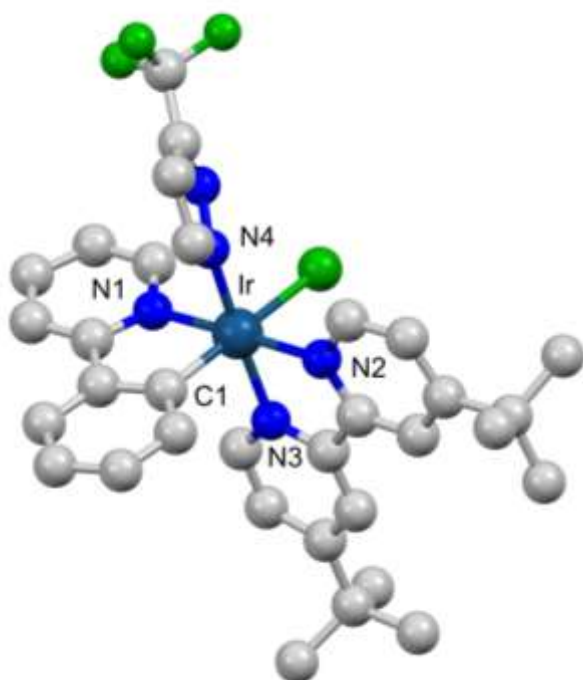


Figure 6. The optimized geometry of one isomer of complex **2'**. Geometrical data: Ir-N(1) = 2.078, Ir-N(2) = 2.070, Ir-N(3) = 2.076, Ir-N(4) = 2.073, Ir-Cl = 2.5957, and Ir-C(1) = 2.020 Å; selected bond angles: N(1)-Ir-C(1) = 80.14, N(2)-Ir-N(3) = 78.44, and N(4)-Ir-Cl = 94.07°.

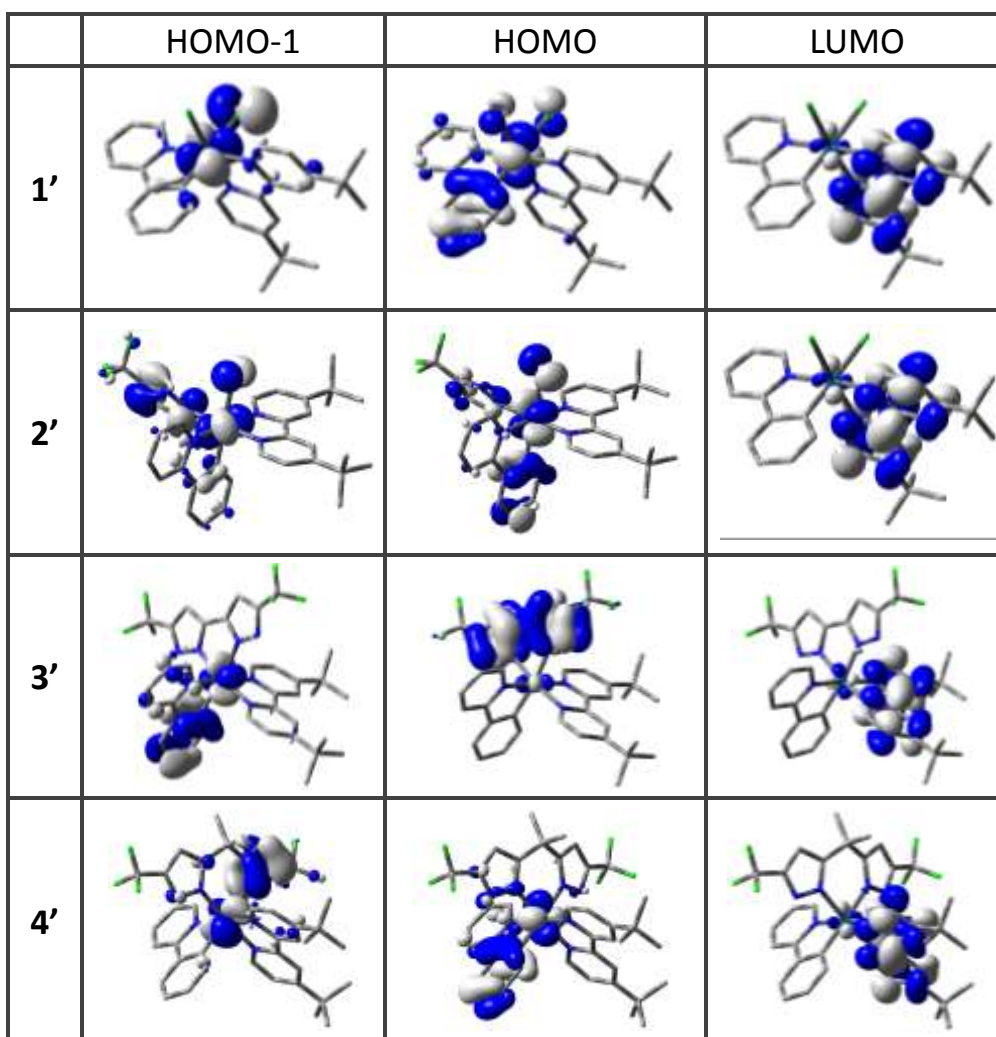


Figure 7. Plots of the HOMO-1, HOMO and LUMO of (a) **1'** (HOMO-1 Ir 50%, Cl 34%; HOMO: Ir 42%, C₆H₄ 33%, Cl 15%; LUMO: bpy 95%) (b) **2'** (HOMO-1 Ir 28%, pz 48%; HOMO: Ir 39%, C₆H₄ 29%, Cl 12%; LUMO: bpy 95%) (c) **3'** (HOMO-1 Ir 31%, C₆H₄ 52%, bipz 3%; HOMO: Ir 4%, bipz 96%; LUMO: bpy 95%) (d) **4'** (HOMO-1 Ir 38%, mepz 51%; HOMO: Ir 32%, C₆H₄ 46%, mepz 10%; LUMO bpy 96%). (All contours are plotted at ± 0.04 (e/bohr³)^{1/2}).

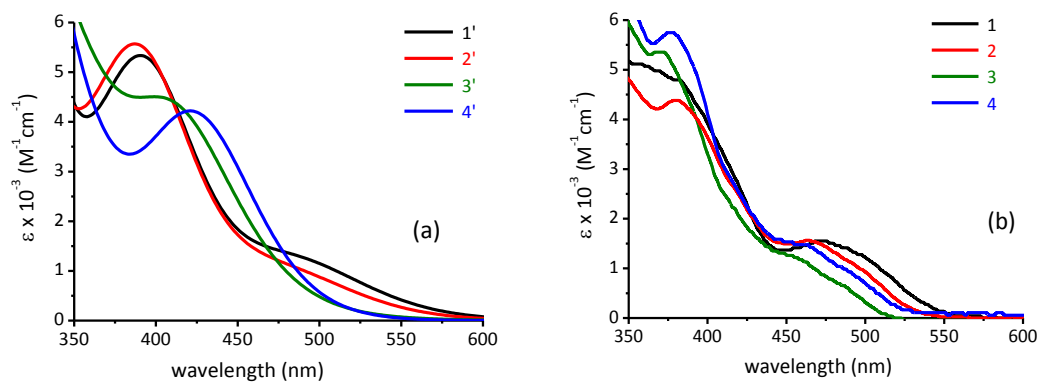


Figure 8. (a) Absorption spectra of complexes **1'** – **4'** simulated from calculated $S_0 \rightarrow S_n$ transitions using half-height band widths of 0.12 eV and molar extinction coefficients (ϵ) from oscillation strengths ($f \times 240000$); (b) the observed spectra of complexes **1** – **4**.

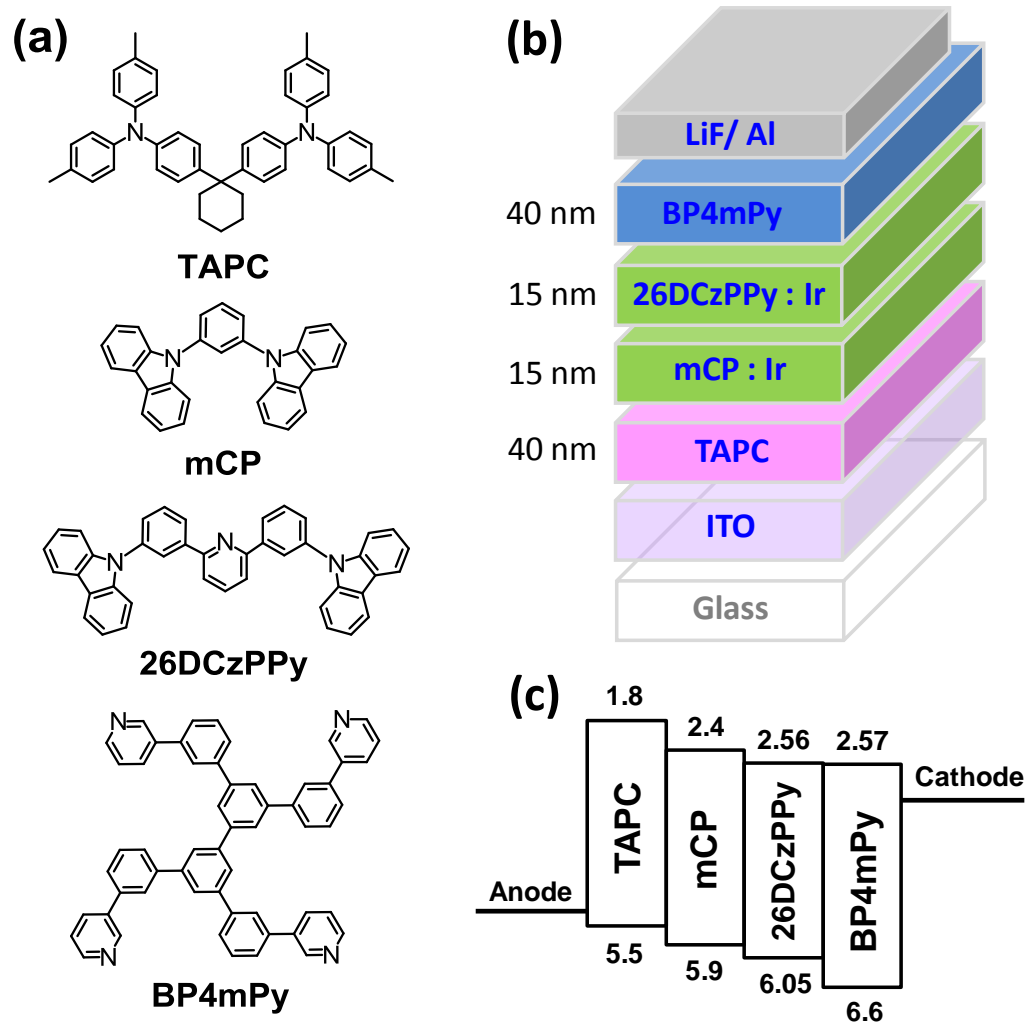


Figure 9. (a) Structural drawings of the chemical materials; (b) schematic device structures and (c) the energy level diagram of the tested green and yellow emitting OLEDs.

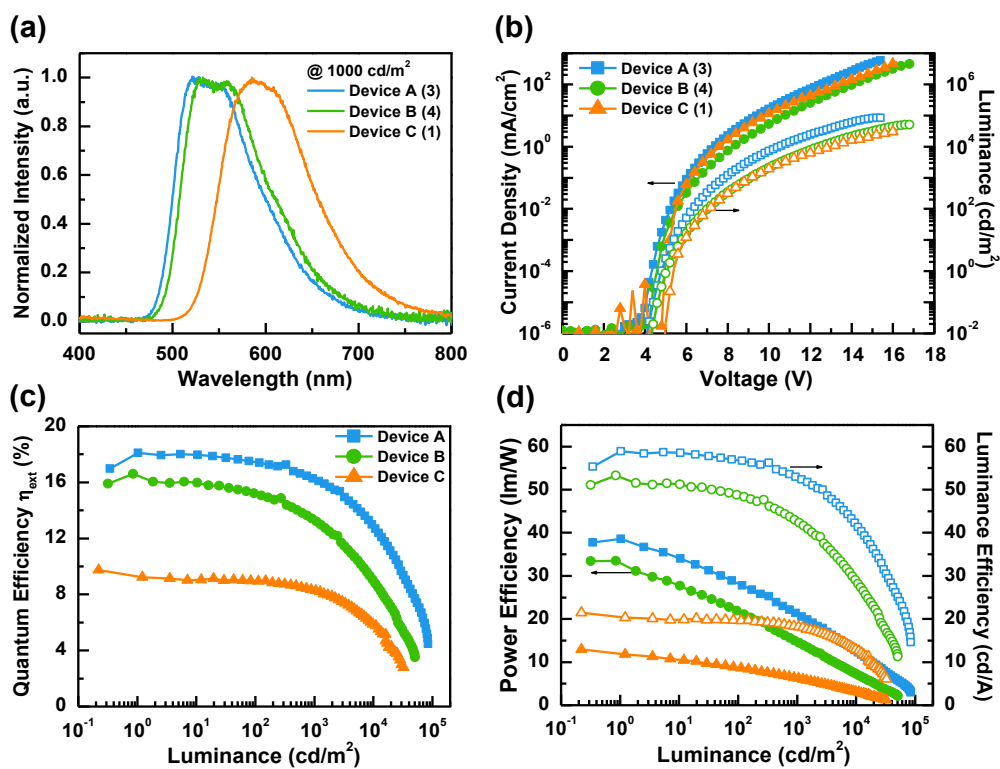


Figure 10. (a) EL spectra of devices with complexes **3**, **4** and **1**; (b) current density-voltage-luminance (J - V - L) curves; (c) external quantum efficiency vs. luminance; (d) power efficiency and luminance efficiency vs. luminance for devices A, B, and C.

Table 1. Photophysical properties for the studied Ir(III) complexes.

	abs. λ_{\max} (nm) [$\epsilon \times 10^{-3}$ ($M^{-1}cm^{-1}$)] ^[a]	PL λ_{\max} (nm) ^[b]	Φ (%) ^[b]	τ (ns) ^[b]	$k_r \times 10^{-5}$ (s^{-1})	$k_{nr} \times 10^{-5}$ (s^{-1})
1	288 [30], 378 [4.8], 468 [1.6]	597 (588)	24 (24)	816 (906)	2.94	9.31
2	284 [32], 378 [4.4], 468 [1.6]	593 (574)	23 (20)	799 (996)	2.88	9.34
3	276 [45], 373 [5.4], 454 [1.3]	546 (532)	27 (73) [70]	355 (1418)	7.60	20.6
4	282 [40], 374 [5.7], 455 [1.5]	546 (545)	76 (88) [79]	2273 (1891)	3.34	1.06

^[a] UV-Vis absorption spectra were measured in 1×10^{-5} M in CH_2Cl_2 . ^[b] Emission spectra were measured in degassed CH_2Cl_2 at RT. Those recorded in PMMA thin film (5 wt.%) and in co-deposited 26DCzPPy (4 wt.%) were marked with parentheses and square brackets, respectively.

Table 2. Electrochemical properties for the studied Ir(III) complexes.^[a]

	$E_{1/2}^{ox}$ (V) [ΔE_p (mV)] ^[a]	E_{pa}^{ox} (V)	$E_{1/2}^{red}$ (V) [ΔE_p (mV)]	E_{pc}^{red} (V)
1	irr	0.80	irr	-2.07
2	irr	0.86	-2.02 [112]	-2.07
3	0.82 [97]	0.87	-1.97 [100]	-2.02
4	irr	0.85	irr	-2.14

^[a] $E_{1/2}$ refers to $[(E_{pa} + E_{pc})/2]$ where E_{pa} and E_{pc} are the anodic and cathodic peak potentials referenced to the FcH^+/FcH couple conducted in CH_2Cl_2 and $\Delta E_p = |E_{pa} - E_{pc}|$.

Table 3. Calculated $S_0 \rightarrow S_1$ and $S_0 \rightarrow T_1$ transition energies (in nm), orbital analysis and photophysical data of **1'** – **4'**. Observed absorption (abs) and emission (em) maxima for **1** – **4** are included for comparison.

	$S_0 \rightarrow S_1$	oscillator strength (<i>f</i>)	$S_0 \rightarrow T_1$	λ_{\max} (abs)	λ_{\max} (em)
1'	484 HOMO \rightarrow LUMO (69%)	0.0219	519 HOMO \rightarrow LUMO (67%)	468	597
2'	478 HOMO \rightarrow LUMO (97%)	0.0176	502 HOMO \rightarrow LUMO (91%)	468	593
3'	512 HOMO \rightarrow LUMO (70%) 449 ($S_0 \rightarrow S_2$) HOMO-1 \rightarrow LUMO (68%)	0.0007 0.0125	516 HOMO \rightarrow LUMO (69%) 474 ($S_0 \rightarrow T_2$) HOMO-1 \rightarrow LUMO (64%)	454	546
4'	453 HOMO \rightarrow LUMO (67%)	0.0053	473 HOMO \rightarrow LUMO (52%) HOMO-1 \rightarrow LUMO (38%)	455	546

Table 4. The EL characteristics of tested PhOLEDs with different emitters.

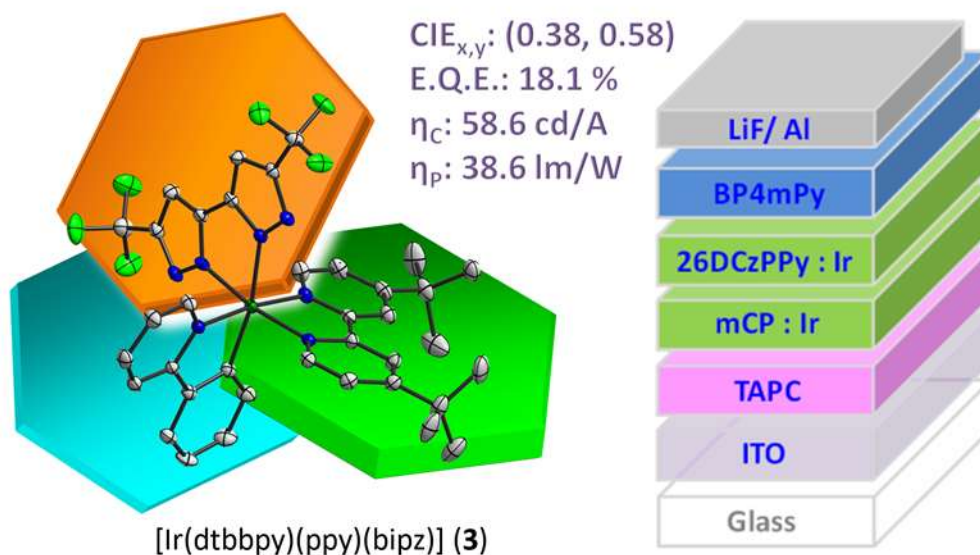
device		A	B	C
emitter		3	4	1
external quantum efficiency (%)	[a]	18.1	16.4	9.8
	[b]	17.6	15.2	9.0
luminance efficiency (cd/A)	[a]	58.6	51.6	21.5
	[b]	57.4	49.9	19.7
power efficiency (lm/W)	[a]	38.6	28.9	13.0
	[b]	30.0	22.4	8.7
V_{on} (V)	[c]	4.8	5.0	5.4
max. luminance (cd/m ²) [voltage]		84899 [15.4 V]	48305 [16.6 V]	32665 [16.2 V]
CIE1931 coordinates	[b]	(0.38, 0.58)	(0.41, 0.56)	(0.55, 0.44)
	[d]	(0.38, 0.58)	(0.41, 0.56)	(0.54, 0.45)

[a] Maximum efficiency; [b] recorded at 10² cd/m²; [c] turn-on voltage measured at 1 cd/m²; [d] measured at 10³ cd/m².

- (1) Zhao, Q.; Li, F.; Huang, C. *Chem. Soc. Rev.* **2010**, *39*, 3007.
- (2) Wong, K. M.-C.; Yam, V. W.-W. *Acc. Chem. Res.* **2011**, *44*, 424.
- (3) Zhou, G.; Wong, W.-Y.; Yang, X. *Chem. Asian J.* **2011**, *6*, 1706.
- (4) Baggaley, E.; Weinstein, J. A.; Williams, J. A. G. *Coord. Chem. Rev.* **2012**, *256*, 1762.
- (5) You, Y.; Nam, W. *Chem. Soc. Rev.* **2012**, *41*, 7061.
- (6) Zhang, X.; Chi, Z.; Zhang, Y.; Liu, S.; Xu, J. *J. Mater. Chem. C* **2013**, *1*, 3376.
- (7) Choy, W. C. H.; Chan, W. K.; Yuan, Y. *Adv. Mater.* **2014**, *26*, 5368.
- (8) Li, G.; Lin, J. *Chem. Soc. Rev.* **2014**, *43*, 7099.
- (9) Yang, X.; Xu, X.; Zhou, G. *J. Mater. Chem. C* **2015**, *3*, 913.
- (10) Wang, Y.; Wang, S.; Shao, S.; Ding, J.; Wang, L.; Jing, X.; Wang, F. *Dalton Trans.* **2015**, *44*, 1052.
- (11) Wang, Y.; Wang, S.; Zhao, N.; Gao, B.; Shao, S.; Ding, J.; Wang, L.; Jing, X.; Wang, F. *Polym. Chem.* **2015**, *6*, 1180.
- (12) Visbal, R.; Gimeno, M. C. *Chem. Soc. Rev.* **2014**, *43*, 3551.
- (13) Lowry, M. S.; Bernhard, S. *Chem. Eur. J.* **2006**, *12*, 7970.
- (14) Zysman-Colman, E.; Denis, C. *Coord. Chem. Rev.* **2012**, *256*, 1742.
- (15) Ladouceur, S.; Zysman-Colman, E. *Eur. J. Inorg. Chem.* **2013**, *2013*, 2985.
- (16) Darmawan, N.; Yang, C.-H.; Mauro, M.; Frohlich, R.; De Cola, L.; Chang, C.-H.; Wu, Z.-J.; Tai, C.-W. *J. Mater. Chem. C* **2014**, *2*, 2569.
- (17) Chi, Y.; Chou, P.-T. *Chem. Soc. Rev.* **2010**, *39*, 638.
- (18) Lee, K. R.; Eum, M.-S.; Chin, C. S.; Lee, S.; Kim, I. J.; Kim, Y. S.; Kim, Y.; Kim, S.-J.; Hur, N. H. *Dalton Trans.* **2009**, 3650.
- (19) Rillema, D. P.; Cruz, A. J.; Moore, C.; Siam, K.; Jehan, A.; Base, D.; Nguyen, T.; Huang, W. *Inorg. Chem.* **2013**, *52*, 596.
- (20) Nguyen, V. H.; Chew, H. Q.; Su, B.; Yip, J. H. K. *Inorg. Chem.* **2014**, *53*, 9739.
- (21) Chou, P.-T.; Chi, Y. *Eur. J. Inorg. Chem.* **2006**, 3319.
- (22) Chou, P.-T.; Chi, Y. *Chem. Eur. J.* **2007**, *13*, 380.
- (23) Chi, Y.; Chou, P.-T. *Chem. Soc. Rev.* **2007**, *36*, 1421.
- (24) Chi, Y.; Tong, B.; Chou, P.-T. *Coord. Chem. Rev.* **2014**, *281*, 1.
- (25) Chi, Y.; Wu, K.-L.; Wei, T.-C. *Chem. Asian J.* **2015**, *10*, 1098.
- (26) Liao, J.-L.; Chi, Y.; Liu, S.-H.; Lee, G.-H.; Chou, P.-T.; Huang, H.-X.; Su, Y.-D.; Chang, C.-H.; Lin, J.-S.; Tseng, M.-R. *Inorg. Chem.* **2014**, *53*, 9366.
- (27) Liao, J.-L.; Chi, Y.; Yeh, C.-C.; Kao, H.-C.; Chang, C.-H.; Fox, M. A.; Low, P. J.; Lee, G.-H. *J. Mater. Chem. C* **2015**, *3*, 4910.
- (28) Hsu, C.-W.; Zhao, Y.; Yeh, H.-H.; Lu, C.-W.; Fan, C.; Hu, Y.; Robertson, N.; Lee, G.-H.; Sun, X.; Chi, Y. *J. Mater. Chem. C* **2015**, DOI: 10.1039/C5TC02261D.

- (29) Yeh, H.-H.; Ho, S.-T.; Chi, Y.; Clifford, J. N.; Palomares, E.; Liu, S.-H.; Chou, P.-T. *J. Mater. Chem. A* **2013**, *1*, 7681.
- (30) Lowry, M. S.; Hudson, W. R.; Pascal, R. A., Jr.; Bernhard, S. *J. Am. Chem. Soc.* **2004**, *126*, 14129.
- (31) Andreiadis, E. S.; Imbert, D.; Pecaut, J.; Calborean, A.; Ciofini, I.; Adamo, C.; Demadrille, R.; Mazzanti, M. *Inorg. Chem.* **2011**, *50*, 8197.
- (32) M'hamedi, A.; Batsanov, A. S.; Fox, M. A.; Bryce, M. R.; Abdullah, K.; Al-Attar, H. A.; Monkman, A. P. *J. Mater. Chem.* **2012**, *22*, 13529.
- (33) Xu, C.; Li, H.-M.; Xiao, Z.-Q.; Wang, Z.-Q.; Tang, S.-F.; Ji, B.-M.; Hao, X.-Q.; Song, M.-P. *Dalton Trans.* **2014**, *43*, 10235.
- (34) Chen, K.; Yang, C.-H.; Chi, Y.; Liu, C.-S.; Chang, C.-H.; Chen, C.-C.; Wu, C.-C.; Chung, M.-W.; Cheng, Y.-M.; Lee, G.-H.; Chou, P.-T. *Chem. Eur. J.* **2010**, *16*, 4315.
- (35) Yoshikawa, N.; Sakamoto, J.; Matsumura-Inoue, T.; Takashima, H.; Tsukahara, K.; Kanehisa, N.; Kai, Y. *Anal. Sci.* **2004**, *20*, 711.
- (36) Soman, S.; Manton, J. C.; Inglis, J. L.; Halpin, Y.; Twamley, B.; Otten, E.; Browne, W. R.; De Cola, L.; Vos, J. G.; Pryce, M. T. *Chem. Commun.* **2014**, *50*, 6461.
- (37) Li, J.; Djurovich, P. I.; Alleyne, B. D.; Tsyba, I.; Ho, N. N.; Bau, R.; Thompson, M. E. *Polyhedron* **2004**, *23*, 419.
- (38) Monti, F.; La Placa, M. G. I.; Armaroli, N.; Scopelliti, R.; Grätzel, M.; Nazeeruddin, M. K.; Kessler, F. *Inorg. Chem.* **2015**, *54*, 3031.
- (39) Liu, S.; Müller, P.; Takase, M. K.; Swager, T. M. *Inorg. Chem.* **2011**, *50*, 7598.
- (40) Chen, Y.-L.; Lee, S.-W.; Chi, Y.; Hwang, K.-C.; Kumar, S. B.; Hu, Y.-H.; Cheng, Y.-M.; Chou, P.-T.; Peng, S.-M.; Lee, G.-H.; Yeh, S.-J.; Chen, C.-T. *Inorg. Chem.* **2005**, *44*, 4287.
- (41) Hung, J.-Y.; Chi, Y.; Pai, I.-H.; Cheng, Y.-M.; Yu, Y.-C.; Lee, G.-H.; Chou, P.-T.; Wong, K.-T.; Chen, C.-C.; Wu, C.-C. *Dalton Trans.* **2009**, 6472.
- (42) Du, B.-S.; Lin, C.-H.; Chi, Y.; Hung, J.-Y.; Chung, M.-W.; Lin, T.-Y.; Lee, G.-H.; Wong, K.-T.; Chou, P.-T.; Hung, W.-Y.; Chiu, H.-C. *Inorg. Chem.* **2010**, *49*, 8713.
- (43) Baranoff, E.; Bolink, H. J.; De Angelis, F.; Fantacci, S.; Di Censo, D.; Djellab, K.; Grätzel, M.; Nazeeruddin, M. K. *Dalton Trans.* **2010**, *39*, 8914.
- (44) Vallett, P. J.; Damrauer, N. H. *J. Phys. Chem. A* **2013**, *117*, 6489.
- (45) Tsepis, A. C. *Coord. Chem. Rev.* **2014**, *272*, 1.
- (46) Xiao, L.; Chen, Z.; Qu, B.; Luo, J.; Kong, S.; Gong, Q.; Kido, J. *Adv. Mater.* **2011**, *23*, 926.
- (47) Chang, C.-H.; Kuo, M.-C.; Lin, W.-C.; Chen, Y.-T.; Wong, K.-T.; Chou, S.-H.; Mondal, E.; Kwong, R. C.; Xia, S.; Nakagawa, T.; Adachi, C. *J. Mater. Chem.* **2012**, *22*, 3832.
- (48) Adachi, C.; Kwong, R.; Forrest, S. R. *Org. Electron.* **2001**, *2*, 37.

- (49) Holmes, R. J.; Forrest, S. R.; Tung, Y.-J.; Kwong, R. C.; Brown, J. J.; Garon, S.; Thompson, M. E. *Appl. Phys. Lett.* **2003**, *82*, 2422.
- (50) Su, S.-J.; Sasabe, H.; Takeda, T.; Kido, J. *Chem. Mater.* **2008**, *20*, 1691.
- (51) Goushi, K.; Kwong, R.; Brown, J. J.; Sasabe, H.; Adachi, C. *J. Appl. Phys.* **2004**, *95*, 7798.
- (52) Su, S.-J.; Tanaka, D.; Li, Y.-J.; Sasabe, H.; Takeda, T.; Kido, J. *Org. Lett.* **2008**, *10*, 941.
- (53) Chang, C.-H.; Wu, Z.-J.; Chiu, C.-H.; Liang, Y.-H.; Tsai, Y.-S.; Liao, J.-L.; Chi, Y.; Hsieh, H.-Y.; Kuo, T.-Y.; Lee, G.-H.; Pan, H.-A.; Chou, P.-T.; Lin, J.-S.; Tseng, M.-R. *ACS Appl. Mater. Int.* **2013**, *5*, 7341.
- (54) O'Brien, D. F.; Baldo, M. A.; Thompson, M. E.; Forrest, S. R. *Appl. Phys. Lett.* **1999**, *74*, 442.
- (55) Baldo, M. A.; Adachi, C.; Forrest, S. R. *Phys. Rev. B.* **2000**, *62*, 10967.
- (56) von Malm, N.; Steiger, J.; Schmechel, R.; von Seggern, H. *J. Appl. Phys.* **2001**, *89*, 5559.
- (57) Chang, C.-H.; Lin, Y.-H.; Chen, C.-C.; Chang, C.-K.; Wu, C.-C.; Chen, L.-S.; Wu, W.-W.; Chi, Y. *Org. Electron.* **2009**, *10*, 1235.
- (58) Sheldrick, G. M. *Acta Crystallogr., Sect. A.* **2008**, *64*, 112.
- (59) Frisch, M. J.; Trucks, G. W.; Schlegel, H. B.; Scuseria, G. E.; Robb, M. A.; Cheeseman, J. R.; Scalmani, G.; Barone, V.; Mennucci, B.; Petersson, G. A.; Nakatsuji, H.; Caricato, M.; Li, X.; Hratchian, H. P.; Izmaylov, A. F.; Bloino, J.; Zheng, G.; Sonnenberg, J. L.; Hada, M.; Ehara, M.; Toyota, K.; Fukuda, R.; Hasegawa, J.; Ishida, M.; Nakajima, T.; Honda, Y.; Kitao, O.; Nakai, H.; Vreven, T.; Montgomery, J. A.; Peralta, J. E.; Ogliaro, F.; Bearpark, M.; Heyd, J. J.; Brothers, E.; Kudin, K. N.; Staroverov, V. N.; Kobayashi, R.; Normand, J.; Raghavachari, K.; Rendell, A.; Burant, J. C.; Iyengar, S. S.; Tomasi, J.; Cossi, M.; Rega, N.; Millam, J. M.; Klene, M.; Knox, J. E.; Cross, J. B.; Bakken, V.; Adamo, C.; Jaramillo, J.; Gomperts, R.; Stratmann, R. E.; Yazyev, O.; Austin, A. J.; Cammi, R.; Pomelli, C.; Ochterski, J. W.; Martin, R. L.; Morokuma, K.; Zakrzewski, V. G.; Voth, G. A.; Salvador, P.; Dannenberg, J. J.; Dapprich, S.; Daniels, A. D.; Farkas, Ö.; Foresman, J. B.; Ortiz, J. V.; Cioslowski, J.; Fox, D. J. *Gaussian 09, Revision D.01; Gaussian Inc.* **2009**, Wallingford.
- (60) Becke, A. D. *J. Chem. Phys.* **1993**, *98*, 5648.
- (61) Stephens, P. J.; Devlin, F. J.; Chabalowski, C. F.; Frisch, M. J. *J. Phys. Chem.* **1994**, *98*, 11623.
- (62) Hay, P. J.; Wadt, W. R. *J. Chem. Phys.* **1985**, *82*, 299.
- (63) Petersson, G. A.; Al-Laham, M. A. *J. Chem. Phys.* **1991**, *94*, 6081.
- (64) O'Boyle, N. M.; Tenderholt, A. L.; Langner, K. M. *J. Comp. Chem.* **2008**, *29*, 839.



Synopsis:

Showcase examples of emissive Ir(III) phosphors, i.e. $[\text{Ir}(\text{dtbbpy})(\text{ppy})(\text{bipz})]$ (**3**) and $[\text{Ir}(\text{dtbbpy})(\text{ppy})(\text{mepz})]$ (**4**), with three distinctive chelates (i.e. neutral, anionic and dianionic) are designed and synthesized. The OLEDs with **3** and **4** as dopants attain peak external quantum efficiencies, luminance efficiencies, and power efficiencies of 18.1% (58.6 cd/A and 38.6 lm/W) and 16.4% (51.6 cd/A and 28.9 lm/W), respectively.